Unlocking microwatt power: enhanced performance of Fe–V–Al thin films in thermoelectric microgenerators

D. Bourgault, H. Hajoum, R. Haettel, E. Alleno

Unlocking Microwatt Power: Enhanced Performance of Fe-V-Al Thin Films in Thermoelectric Microgenerators

D. Bourgault[(1,2) *], H. Hajoum[(1,2)], R. Haettel[(1,2)], E. Alleno[(3)]

[(1)] Univ. Grenoble Alpes, Institut Néel, F-38042 Grenoble, France.

[(2)] Centre National de la Recherche Scientifique / Institut Néel, 25 Avenue des Martyrs, BP 166, 38042 Grenoble Cedex 9, France

[(3)] Univ. Paris Est Creteil, CNRS, ICMPE, UMR 7182, 2-8, rue H. Dunant, F-94320 Thiais, France

* Corresponding author ; E-mail : daniel.bourgault@neel.cnrs.fr ;

Abstract :

Microwatt power output was obtained in thermoelectric microgenerators based on cost-effective and non-toxic Fe-V-Al thin films deposited by a DC magnetron co-sputtering process. A maximum electrical power of almost 5 µW at a temperature difference of 134 K was measured. This result leads to a maximum power density of 58.5 ± 6 mW/cm^2, which is among the highest values obtained by a microdevice. Contrary to what is observed for other thermoelectric materials like Bi_2Te_3 or PEDOT composites, the performances of the present devices, assembled with junctions between Fe-V-Al and aluminum electrodes, are weakly impacted by their contact resistance. These results are very encouraging for the development of new architectures based on low-resistance Fe-V-Al thin films to power autonomous sensors in the Internet of Thing domain.

Keywords : thermoelectric device, thermoelectrical thin film, Fe_2VAl, dc magnetron sputtering, contact resistance.

1. Introduction

Despite advancements in the fields of manipulating new compositions and nanostructuring known compounds [1,2], there has been limited research on fabricating devices for micropower generation or thermoelectric microcooling using inexpensive, abundant, and non-toxic materials [3-4]. Micropower generation is of great interest in autonomous electronic microsystems that require local renewable energy sources. Thermoelectric energy harvesters can be used in applications such as local networks of microcontrollers, sensors, and wireless communication chips. Additionally, microdevices find application in sensing tasks like measuring infrared radiation, vacuum, airflow, and heat flow [5-8].

The intrinsic properties of thermoelectric materials, such as the Seebeck coefficient (S), electrical resistivity (ρ), and thermal conductivity (λ), determine the performances of the (micro)generators based on them. Indeed, in transverse geometry, their efficiency at temperature T is determined by the dimensionless figure of merit ($ZT = S^2T/(\rho\lambda)$) of the *p*- and *n*-type materials constituting these devices. The maximum output power P_{max} of these devices is given by

$$P_{max} = \frac{V_{open}^2}{4R_{internal}} = \frac{x^2(S_p - S_n)^2 \Delta T^2}{4R_{internal}} = \frac{x^2(S_p - S_n)^2 \Delta T^2}{4(R_{thermo} + R_{contact})} \quad (1)$$

It is related to V_{open}, which is the generated output voltage in open circuit depending on x the number of *n*-*p* couples, the Seebeck coefficient of the *p*- and *n*-type materials (S_p and S_n respectively) and the temperature difference ΔT. P_{max} is also depending on $R_{thermo,}$ the thermoelectric thin films resistance and $R_{contact}$, the contact resistance between the thermoelectric materials and the metal electrodes that collect the electrical current. This last parameter is crucial for microgenerator performance. While bismuth - antimony - telluride (*p*-type) and bismuth - selenium - telluride (*n*-type) are materials commonly used for thermoelectric applications near room temperature because of their large $ZT = 1$, the generated

power is limited due to contact resistance issues between thin films of bismuth telluride and electrodes.

Existing literature describes microgenerators based on various materials [9-29]. However, to the best of our knowledge, there is no microdevice based on the full-Heusler alloy [30] Fe_2VAl under thin film form. Only a few devices based on bulk Fe_2VAl have been reported [31,32]. Notably, Mikami et al. developed generators based on sintered Fe_2VAl alloys, which achieved a maximum output power of 1.2 W for a temperature difference (ΔT) of 280 K [31], latter improved to 2.5 W by Sb doping [32]. Fe_2VAl is made of inexpensive and non-toxic elements and it exhibits power factor ($P_F = S^2/\rho$) values larger than in Bi_2Te_3 [33-35]. However, its high thermal conductivity (~28 W/mK) [36] results in a moderate ZT value. As a consequence, the thermoelectric energy conversion efficiency using bulk materials is considerably lower than that of state-of-the-art thermoelectric materials. Nevertheless, by utilizing thin films, the drawback of a high thermal conductivity is partially mitigated by the thermal properties of the substrate, when the temperature gradient is parallel to the substrate plane, in the so-called "planar geometry" (Fig. 2). Recent research demonstrated the successful production of Fe_2VAl thin films using magnetron co-sputtering, exhibiting good performances at room temperature with power factors of 5.6 mW/K^2m and 1.3 mW/K^2m for *n*-type and *p*-type, respectively [37]. These values are very close those observed in bulk alloys [34, 38, 39].

The study presented in this article highlights that dc magnetron co-sputtering is a suitable process for fabricating Fe-V-Al thermoelectric devices. Two microgenerators consisting of five *n-p* couples deposited on Al_2O_3 and AlN substrates respectively, were fabricated and tested. The low contact resistance achieved using aluminum as an electrode material contributed to a low internal resistance, enabling the demonstration of a maximum power of 5 μW for a temperature difference of 134 K, corresponding to a normalized power density of 3.3 $\mu W/cm^2K^2$.

2. Experimental

The sputtering conditions for *n*- and *p*-type Fe_2VAl were investigated in a precedent work [37]. It revealed that the best power factor is obtained for thin films deposited at 600 °C under an Ar flow of 40 sccm and under a pressure of 10^{-2} mbar. Figure 1a shows the sputtering chamber in which the three targets are visible. The co-sputtering process is schematically explained in figure 1b. It is required to finely tune the compositions and subsequently, the thermoelectric properties.

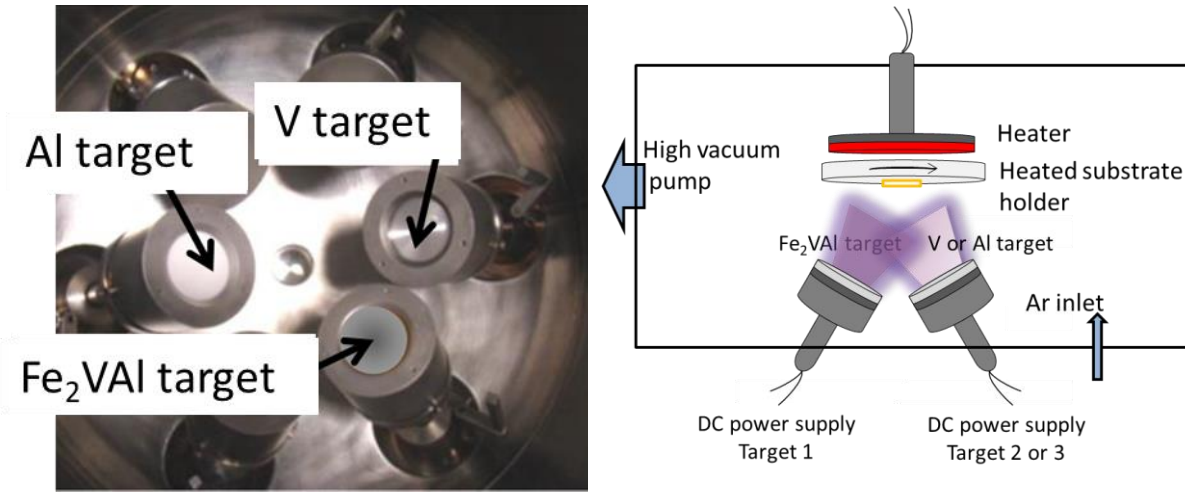

a) **b)**

Figure 1 : a) Image showing the sputtering chamber with the three targets used for composition tuning of Fe-V-Al thin film . b) Co-sputtering process scheme.

Film compositions were accurately determined using Energy Dispersive X-ray Spectroscopy (EDS) with a precision of ± 1 atomic %.

Seebeck coefficient, *S*, of the films is measured with home-made devices described in Reference [40]. The electrical resistivity (ρ) was obtained using the van der Pauw method and the relationship $\rho = K \times R \times e$ with $K = \pi / \ln 2 = 4.53$, R represents the measured electrical resistance, and e denotes the film thickness.

To fabricate the devices consisting of interconnected *n*- and *p*-type legs in series, mechanically machined masks (Figure 2) were implemented. Elemental aluminum deposition was employed for the contacting electrodes between the *n*-type and *p*-type thermoelectric legs. As illustrated in Figure 2, aluminum pads were deposited *on* the *n*-type and *p*-type legs. The contact resistance is hence reduced compared to the situation where the Fe_2VAl films are deposited *on* the aluminum pads. In this case, electrical measurements showed contact resistances 4 to 5 orders of magnitude higher. This discrepancy is likely due to the Fe_2VAl's lower sensitivity to oxidation compared to aluminum. To gain insight into the mechanisms governing low contact resistivities, microstructural observations and chemical analysis of the Fe_2VAl-Al and Al-Fe_2VAl interfaces will be conducted. Additionally, the Transfer Length Method (TLM) will be employed to precisely measure the contact resistivity. We plan to explore various metals, with or without very thin bonding layers (e.g., Ti, a few nm thick), and utilize ion etching before Al deposition to test ways of reducing contact resistivity.

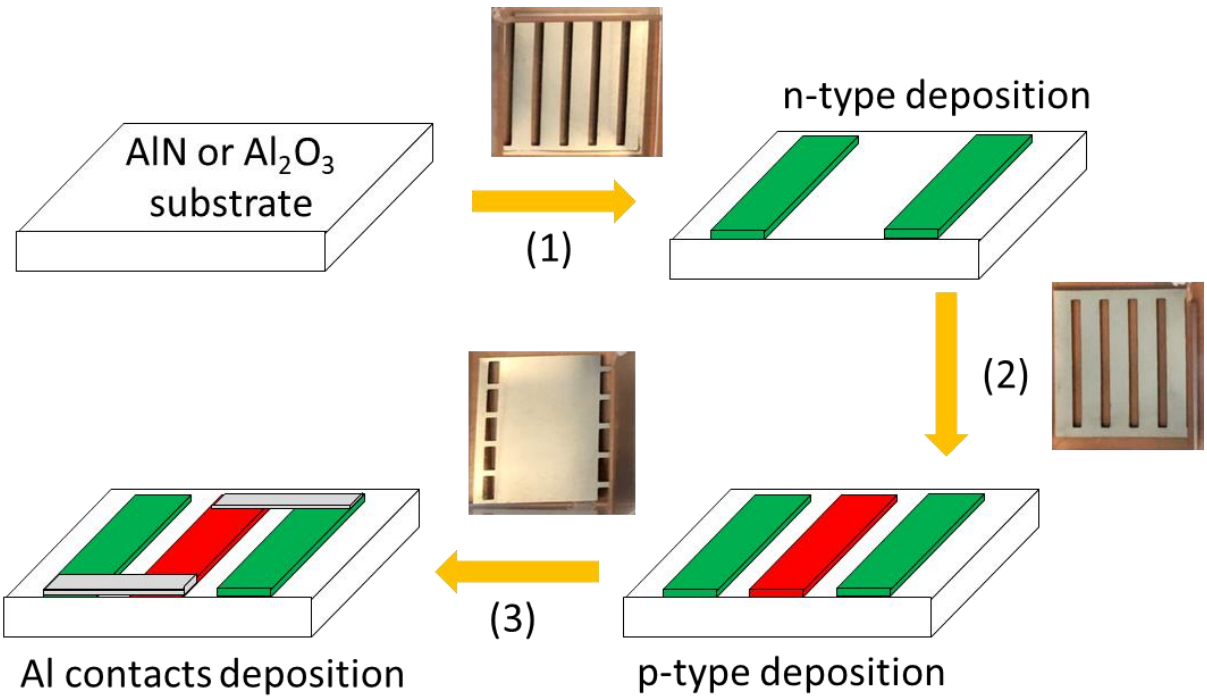

Figure 2: Scheme of the *n*-type and *p*-type legs with aluminum joints, assembled in the planar device. Pictures of the machined masks implemented at the three deposition stages are also displayed.

The measurement setup of the device enables the application of a temperature difference along the plane of the deposited thin films (Figure 3a). The hot zone, located on the left side of the device, was controlled using a heating cartridge, while the cool zone on the right side was maintained at a constant temperature of 17 °C by circulating water. To measure the generated voltages, induced by various temperature differences (ΔT) ranging from 20 K to 134 K, a 34401A Agilent voltmeter with a 10 GΩ impedance was utilized.

Temperature profile measurements were conducted using a FLIR A655sc thermal camera with a resolution of 640 × 480 pixels (see Figure 3b and 3c).

The choice of substrates with different thermal conductivities, Al_2O_3 and AlN, has a notable impact on shaping the temperature difference in the thermoelectric microgenerator system. The thermal conductivity of Al_2O_3 is approximately 20 W/mK, while AlN has a significantly higher thermal conductivity of around 180 W/mK. Due to this substantial difference, when subjected to the same heat source at one end, the Al_2O_3 substrate exhibits a much steeper temperature gradient compared to AlN. This occurs because the thermoelectric layer deposited on the surface of the substrate is relatively thin (around 500 nm) in comparison to the substrate's thickness (around 500 microns). As a result, the temperature gradient is predominantly governed by the substrate, even when the thermal conductivities of the Fe_2VAl thermoelectric layers range from 20-30 W/mK. Simulations carried out in reference [41] have shown that as long as the thermoelectric layers remain thin compared with the substrate, the thermal contributions are mainly linked to the substrate and the performance of the system is governed by the P_F rather than the ZT as is the case for bulk materials.

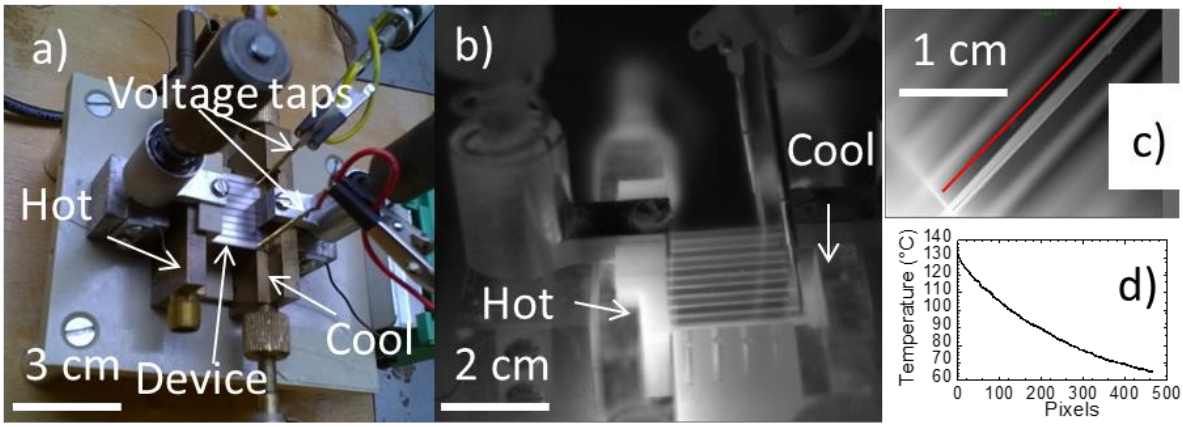

Figure 3 : Visible (a) and thermal (b) images of a five *n-p* couple device mounted on the sample holder. Magnified thermal image (c) and thermal profile (d) along a direction parallel to the n and p legs (red line).

3. Thermoelectrical performances

Before device assembling, the thermoelectric properties of the *n*-type and *p*-type thin films were investigated.

Table 1 summarizes the Seebeck coefficient, the electrical resistivity and the power factor previously obtained on the films whereas Table 2 details the deposition conditions such as plasma power, deposition time, Ar pressure, target-substrate distance, and deposition temperature for both *n*- and *p*-type thin films. In reference [37], a strong improvement in power factor was achieved by implementing the co-sputtering process at a deposition temperature of 600 °C for the *n*-type thin film. The essential parameter with a significant influence on film composition is the plasma power applied to the secondary Al or V target, while maintaining a fixed power on the main Fe_2VAl target. Through this co-sputtering process, we observed a linear variation of the atomic composition, depending on the nature and power applied to the secondary target [37]. This enabled precise tuning of the film composition, spanning from the stoichiometric $Fe_{2.01}V_{0.99}Al$ to Al-rich $Fe_{1.90}V_{0.88}Al_{1.22}$ and to V-rich $Fe_{1.90}V_{1.24}Al_{0.86}$.

Analyzing the Seebeck coefficient and power factor variations versus the valence electron concentration (VEC), calculated from film compositions, we identified a maximum at VEC values slightly above and below 6 for n-type and p-type films, respectively. The power factors reached were 5.6 and 1.3 mW/K^{2}m for the V-rich *n*-type film ($Fe_{1.97}V_{1.15}Al_{0.88}$) and the Al-rich *p*-type film ($Fe_{1.94}V_{0.94}Al_{1.12}$), respectively. In the near future, the films showing high power factors will be measured in magnetic susceptibility. In a recent study, Gao et al. have observed that Ti doped Fe_2VAl thin films are ferromagnets distinctly different from the paramagnetic state of bulk sample [42]. The good thermoelectric properties obtained in our V-rich *n*-type film ($Fe_{1.97}V_{1.15}Al_{0.88}$) and the Al-rich *p*-type film ($Fe_{1.94}V_{0.94}Al_{1.12}$) may be due to such magnetic interactions via spin fluctuation as shown in [43].

	Seebeck coefficient, S (µV/K)	**Electrical resistivity, ρ (µΩ.m)**	**Power factor, PF ($mW.m^{-1}K^{-2}$)**
$Fe_{1.94}V_{0.94}Al_{1.12}$ (*p*-type)	+55	2.4	1.3
$Fe_{1.97}V_{1.15}Al_{0.88}$ (*n*-type)	-96	1.6	5.6

Table 1 : Seebeck coefficient, electrical resistivity and power factor for *p*-type and *n*-type Fe-V-Al thin films.

4. Devices with five *n-p* couples

Two devices were constructed, each composed of five junctions electrically connected in series on the AlN substrate (Figure 4a) and the Al_2O_3 substrate (Figure 4b). The five n-p pairs within each device were interconnected using aluminum junctions.

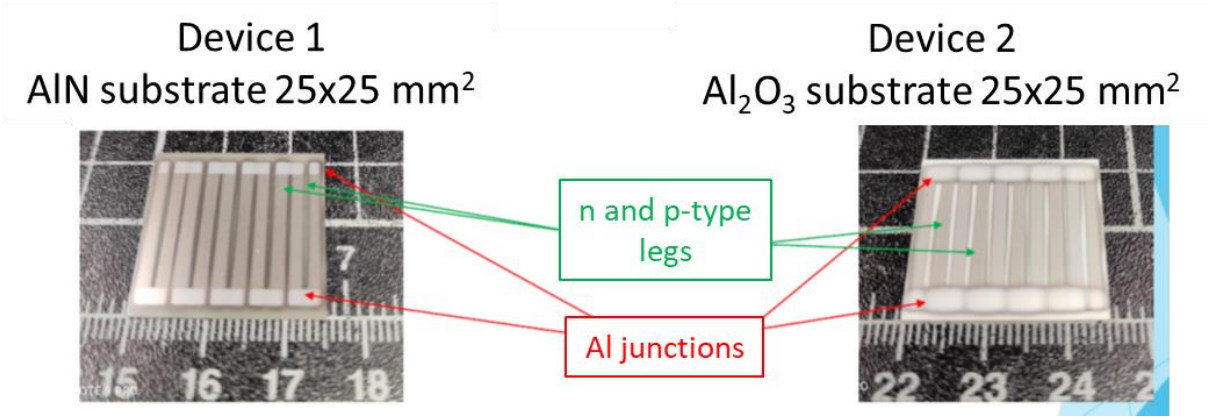

a) b)

Figure 4 : Pictures of the two devices deposited on AlN (a) and Al_2O_3 substrates (b).

	***n*-type deposition**	***p*-type deposition**	**Al contact deposition**	**Device 1**	**Device 2**
Substrate				AlN	Al_2O_3
Plasma power Fe_2VAl target (W)	137	137	0		
Plasma power Al target (W)	0	16	50		
Plasma power V target (W)	16	0	0		
Temperature deposition (°C)	600	600	20°C		
Time deposition (hour)	1	1	2		
Dimensions (cm) L	2.2	2.2			
l	0.18	0.18			
e	$4.5\ 10^{-5}$	$5\ 10^{-5}$			
Number of legs	5	5			
Calculated R_n and R_p (Ω) for one leg	43	59			
Calculated resistance R_{thermo} (Ω)				510	510
Measured resistance (Ω)				586	554

Table 2 : Deposition conditions for *n*-type, *p*-type Fe-V-Al and Al thin films, calculated and measured resistances of devices 1 and 2.

The optimal deposition conditions presented in Table 2 were implemented for the fabrication of the two devices, to achieve the highest power factor and maximum voltage generated by a given temperature difference. Table 2 also displays the calculated resistance based on the electrical resistivity and dimensions of both n-type and p-type legs, as well as the measured resistances at room temperature using the 4-point probe method for both devices. It is worth noting that the measured resistances for both devices slightly deviate from the calculated resistance R_{thermo} based on the electrical resistivities of the films and the assembly design. This difference is ascribed to the total contact resistance, $R_{contact}$, between the aluminum and thermoelectric thin films, as described by equation (2).

Equation (2) $$R_{int\,ernal} = R_{thermo} + R_{contact} = x(R_n + R_p) + R_{contact}$$

where x represents the number of n- and p- couples, here $x = 5$. R_n and R_p are the resistance of a single n-type and p-type leg, respectively. $R_{contact}$ and ρ_c are related by the relation $R_{contact} = \frac{4x\rho_c}{A_{contact}}$ with A_{contact} the surface of contact between the metal and the thermoelectric thin films.

5 Tests of the devices

5.1 Temperature difference measurement

The temperature difference ΔT was determined by analyzing the thermal profile recorded by the IR camera on the thermoelectric legs (Figure 3c). To ensure accurate temperature measurements with the IR camera, the emissivity (ε) of the thermoelectric films must be determined. This was performed beforehand using small K-type thermocouples on legs dedicated to these thermal measurements. The temperature differences determined by the thermocouples and those using the IR camera were in agreement when the emissivity was set to the value $\varepsilon = 0.85$. In Figures 3c and 3d, a magnification of the thermal image and the thermal profile measured along the direction (indicated by the red line) parallel to the n and p legs is

shown. In this specific case, the temperature difference along the *n-p* couples is ΔT = 130.5 - 64.5 = 66 K.

5.2 Generated output voltage in open circuit V_{open}

Figure 5 illustrates the output voltage (V_{output}) generated by devices 1 (AlN substrate) and 2 (Al_2O_3 substrate) in open circuit condition (V_{open}), for various temperature differences. Device 2 exhibits a generated voltage exceeding 110 mV for a temperature difference of 134 K. For device 1, the slope of the voltage-temperature curve is 0.80 mV/K, resulting in a mean Seebeck coefficient of 160 µV/K for each couple of the device. Despite the higher temperature difference applied along the Al_2O_3 substrate in device 2, the slope of V_{open} versus ΔT is 0.83 mV/K, which is similar to the value observed for device 1. These results are in good agreement with the Seebeck coefficients measured in the *p*- and n-type thin films deposited on the MgO substrate, as reported in Table 1: +55 µV/K and -96 µV/K, respectively, yielding a Seebeck coefficient of 151 µV/K for a couple.

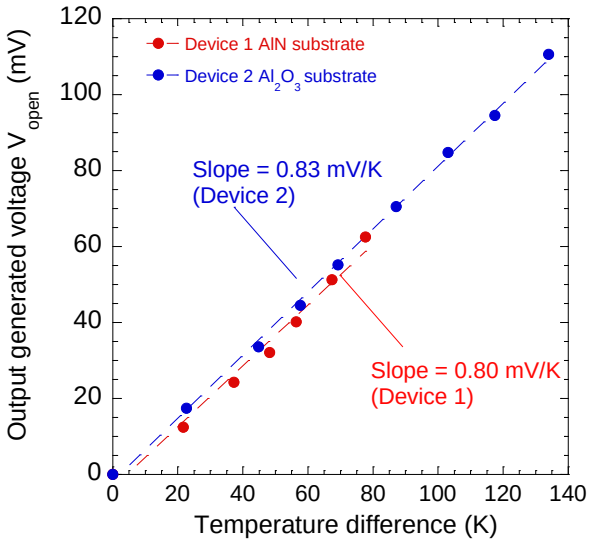

Figure 5 : Output generated voltages in open circuit condition, versus temperature differences applied along devices 1 and 2.

5.3 Generated electrical power

Figures 6a and 6b show the output voltage and power generated by device 1 and device 2, respectively, for various connected resistive loads at several temperature differences. When a load is connected to the thermoelectric device, the voltage decreases due to the presence of the internal electrical resistance ($R_{internal}$). For device 1, a current of 92 μA is generated at a temperature difference of 78 K, while for device 2, a current of 180 μA is generated at a temperature difference of 134 K. The values of internal resistance and current (I) are calculated using Equation (3) as follows:

Equation (3)

$$R_{internal} = \frac{V_{R\,internal}}{I} = \frac{V_{open} - V_{output}}{V_{output} / R_{load}}$$

Based on the values provided in Table 2, the calculated R_{thermo} is 510 Ω, which is lower than the measured values of 586 Ω and 554 Ω for devices 1 and 2, respectively. The interfaces between Al and the thermoelectric thin films contribute approximately to 13% (8% for device 2) of the internal resistance. Considering the 20 Al-thermoelectric thin film junctions with a connected surface area $A_{contact}$ of approximately 4 mm^2, the areal contact resistance ρ_c is estimated to be around 152 $m\Omega \cdot cm^2$ for device1 and 88 $m\Omega \cdot cm^2$ for device 2. It is worth noting that this contribution is relatively small compared to what is typically observed in devices consisting of bismuth telluride thin films. In such cases, the contact resistance is often 2 to 5 orders of magnitude larger than the resistance of the thin films themselves [13]. The variations in areal contact resistance (ρ_c) between the two devices can be primarily attributed to the distinct average roughness (Ra) of the AlN and Al_2O_3 substrates. This disparity in surface roughness necessitates consideration of the real areal contact ($A_{contact}$) when calculating ρ_c to avoid errors in the measurements. Additionally, the presence of porosity on the substrate's surface, which

can vary depending on its roughness, may also influence the current flow between the metal and thermoelectric thin film.

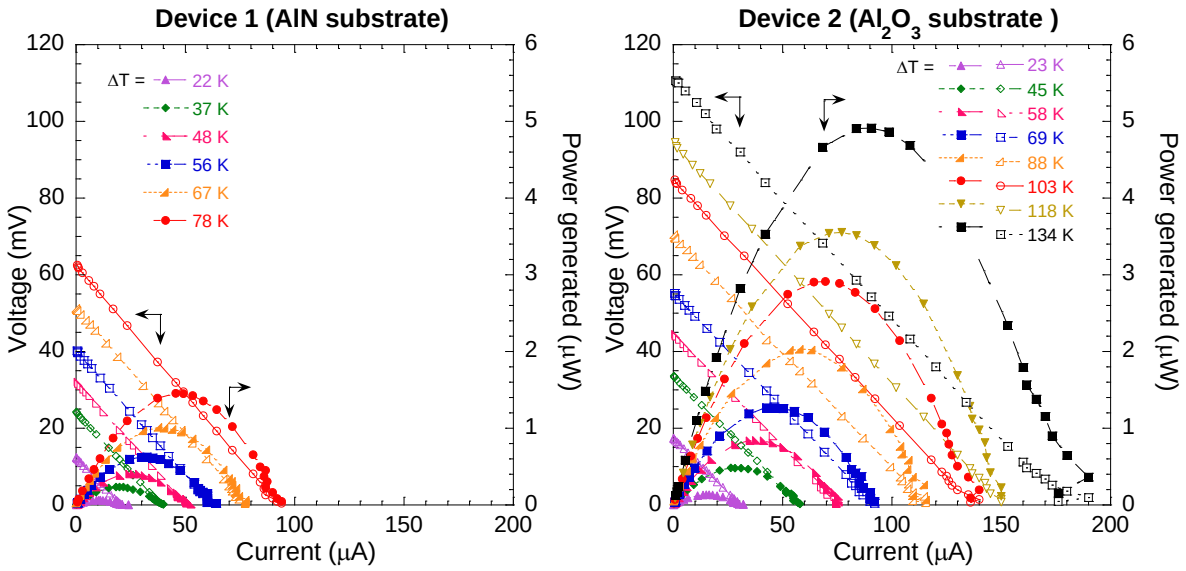

Figure 6: Generated voltage and power for various temperature differences applied to devices 1 (a) and device 2 (b). Open symbols are voltage data (left axis) and filled symbols are power data (right axis).

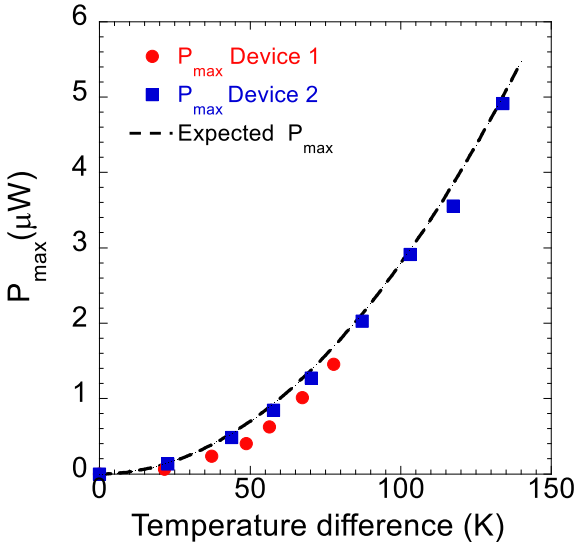

Figure 7 : Variation of the maximum power generated for various temperature differences for devices 1 (in red) and 2 (in blue). Expected law $P_{max} = x^2(S_p$ -

$S_n)^2\Delta T^2/4R_{internal}$ with x = 5, S_p - S_n = 151 μV/K and $R_{internal}$ = 510 Ω with zero contact resistance (dashed black lines).

The maximum electrical power, P_{max}, achieved is 5 μW for a temperature difference of 134 K in device 2. Figure 7 illustrates the relationship between the maximum power generated and different temperature differences for both devices. The observed variation follows the expected theoretical law based on equation (1) with 5 couples, S_p - S_n = 151 μV/K and $R_{internal}$ = 510 Ω with zero contact resistance. There is a slight deviation between the experimental data and the fitted curve for device 1, which can be attributed to the contribution of the contact resistance of 13% to the internal resistance whereas it is only 8% for device2. These values hold significant promise for Internet of Things (IoT) applications. Considering the cross-sectional area $A = l \times e$ for *n*- and *p*-type legs for heat flow and the number of couples (five), a maximum power density of approximately 58.5 ± 6 mW/cm^2 is thus achieved for ΔT = 134 K.

Figures 8a and 8b provide a comprehensive comparison of the maximum power density and normalized power density for various planar devices developed using different thermoelectric materials. The power density results from microdevices based on various materials, which include Bi-Sb-Te-Se-based ones (shown in blue) [13, 41-52], organic composite-based ones (shown in black) [53-58], AgSe-based one (shown in green) [59-62], and our Fe_2VAl thin films (shown in red). Notably, our Fe_2VAl thin films deposited on a Al_2O_3 substrate exhibit an exceptionally high power density of 58.5 ± 6 mW/cm^2 for a temperature difference of ΔT = 134 K, surpassing the values reported in the literature.

To facilitate a fair comparison across differing temperature gradients, the normalized power density $\frac{P_{max}}{(\Delta T)^2}$ is depicted in Figure 8b. Again, it is worth noting that our device2, fabricated using Fe_2VAl thin films on Al_2O_3 substrate, demonstrates a remarkable normalized power density of

3.3 ± 0.7 μW/cm^{2}K^2, higher than the values found in organic and inorganic thermoelectric materials investigated thus far.

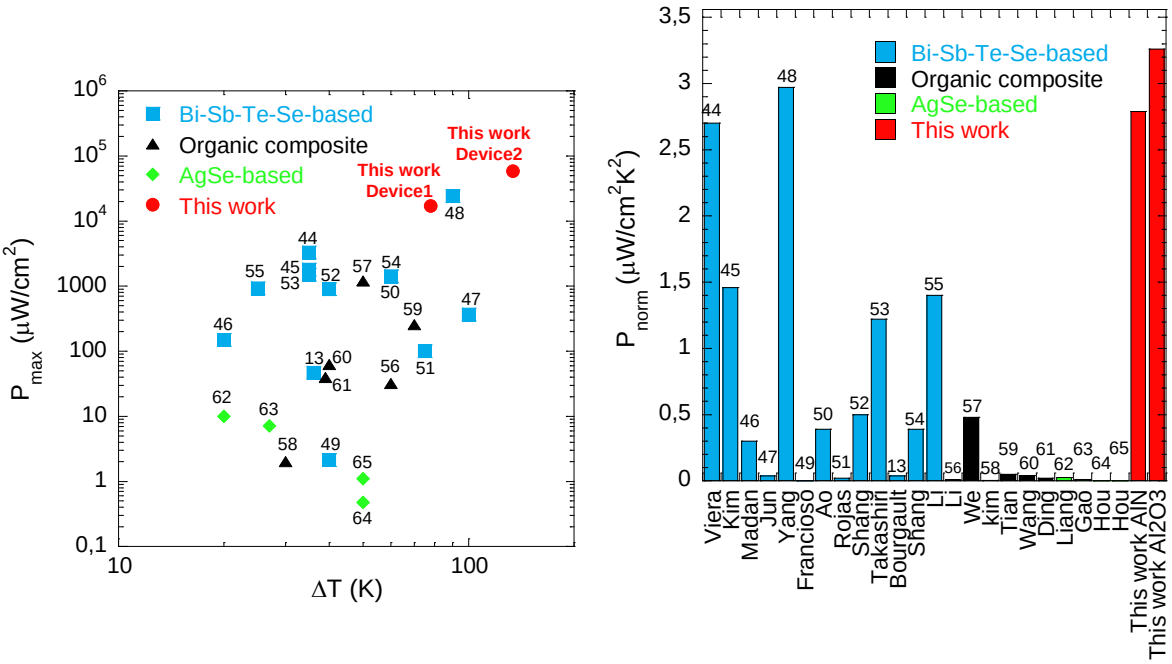

a) b)

Figure 8 : (a) Maximum power density and (b) normalized power density of this study in comparison to state-of-the-art for planar devices (Bi-Sb-Te-Se-based in blue [13, 44-55], organic composite-based in black [56-61] and AgSe-based in green [62-65]).

In a study conducted by Mikami et al., a normalized power generation density of 1.27 μW/cm^{2}K^2 was calculated using the cross-sectional area of thermoelectric bulk-Fe_2VAl under a temperature difference of ΔT = 280 K [31]. By incorporating Sb doping, the normalized power density increased to 2.55 μW/cm^{2}K^2 [32]. Our obtained values are comparable or slightly higher, indicating that our thin film devices are highly competitive, and that the contact resistance does not significantly impair their performance.

It is also worth noting that when considering the effective planar area $2x \times L \times l$ (not the cross-sectional area $2x \times A$), the planar power density is approximately 1.2 μW/cm^2. By accounting for the temperature difference to compare several devices, the effective planar power density is

close 9 nW/cm^{2}K. This value is similar to the power densities achieved in planar thin film devices based on Bi_2Te_3/Sb_2Te_3 (ranging from 3 to 10 nW/cm^{2}K) [11, 44, 48, 51, 66] and sustainable materials (ranging from 0.3 to 1.9 nW/cm^{2}K) [66].

These results highlight the competitive performance of our thin film devices, demonstrating their potential for practical thermoelectric applications, comparable to established materials such as bismuth tellurides and other sustainable materials.

5. Conclusion

We have reached a significant milestone by measuring microwatt as electrical power output in thermoelectric microgenerators utilizing high-efficiency Fe-V-Al *n*- and *p*-type films. These films are synthesized by a dc magnetron co-sputtering process, enabling precise composition control and optimization of the electronic transport performance, as evidenced by a power factor (P_F) of 5.6 and 1.3 mW/m^{2}K for the *n*-type and *p*-type thin films, respectively. Notably, our microdevices exhibit a remarkable maximum power generation of approximately 5 μW, achieved with a temperature difference of 134 K.

The performance of these microdevices, when assembled with a simple Al junction, shows no significant degradation from the contact resistance. This stands in contrast to the commonly encountered challenges faced by microdevices employing other thermoelectric materials such as Bi_2Te_3 or PEDOT compounds. These findings offer great promise for the development of innovative architectures based on low-resistance Fe-V-Al thin films, enabling the power supply for autonomous sensors in the rapidly growing Internet of Things (IoT) domain. Moreover, these results not only contribute to the advancement of thermoelectric technologies but also underscore the feasibility of employing cost-effective and environmentally friendly Fe-V-Al thin films as a viable alternative in the field of energy harvesting and microsystems.

Acknowledgments :

This work has been partially funded by the CNRS Energy unit through the project COMITHER (n° EDP121268) and by the "Agence Nationale de la Recherche" through the contract ''LoCoThermH'' (Project ANR-18-CE05-0013-01). The authors thank A. Gerardin (Pôle Cryogénique) and G Perroux (SERAS) from the Institut Néel for the mechanical facilities. They also thank N. Caillault and S. Giraud from Schneider Electric for access to their sputtering equipment and for profilometer measurements.

References

[1] X. L. Shi, J. Zou, Z. G. Chen. "Advanced Thermoelectric Design: From Materials and Structures to Devices." Chem. Rev., 2020, 120, 7399−7515.

[2] K. V. Selvan, M. N. Hasan, M. S. Mohamed Ali. "State-of-the-Art Reviews and Analyses of Emerging Research Findings and Achievements of Thermoelectric Materials over the Past Years." Journal of Electronic Materials, 2019, 48, 745-777.

[3] Y. Li, G. Wang, M. Akbari-Saatlu, M. Procek, H. H. Radamson. "Si and SiGe nanowire for micro-thermoelectric generator: A review of the current state of the art." Frontiers in Materials, 2021, 8, 611078.

[5] F. Völklein. "Thermal-based microsensors." In MEMS-A Pratical Guide to design, Analysis and Application, William Andrew, 2006 (Chapter 5).

[6] W. Shin, M. Nishibori, L.F. Houlet, T. Itoh, N. Izu, I. Matsubara. "Fabrication of thermoelectric gas sensors on micro-hotplates". Sensors and Actuators B, 2009, 139, 340-345.

[7] Z. Xiao, X. Zhu. "On-Chip Sensing of Thermoelectric Thin Film's Merit". Sensors, 2015, 15, 17232-17240.

[8] A. Bali, R. Chetty, R. C. Mallik. "Thin Film Structures in Energy Applications." Chapter 7, 2015, 215.

[9] J. Yan, X. Liao, Y. Chen. "Review of Micro Thermoelectric Generator." J Microelectromech Syst, 2018, 7, 1-18.

[10] J. Zhang, W. Zhang, H. We, J. Tang, D. Li, D. Xu. "Flexible micro thermoelectric generators with high power density and light weight." Nano Energy, 2023, 105, 108023.

[11] D. Tainoff, A. Proudhom, C. Tur, T. Crozes, S. Dufresnes, S. Dumont, D. Bourgault, O. Bourgeois. "Network of thermoelectric nanogenerators for low power energy harvesting." Nano Energy, 2019, 57, 804–810.

[12] G. Moiroux, C. Tur, D. Bourgault, J.-L. Garden. "High temperature difference in a new flexible thermoelectric bismuth telluride microgenerator." Sensors and Actuators: A. Physical, 2022, 347, 113961 p1-7.

[13] D. Bourgault, C.G. Garampon, N. Caillault, L. Carbone. "Thermoelectrical devices based on bismuth-telluride thin films deposited by direct current magnetron sputtering process." Sens. Actuators A, 2018, 273, 84–89.

[14] C. B. Vining. "Semiconductors are cool." Nature, 2001, 413, 577-578."

[15] A. Majundar. "Thermoelectricity in semiconductor nanostructures". Science, 2004, 303, 777-778.

[16] G. Chen, M. S. Dresselhaus, G. Dresselhaus, J. P. Fleurial, T. Caillat, "Recent developments in thermoelectric materials". Int. Mater. Rev., 2003, 48, 1.

[17] W. Qu, M. Plötner, W. J. Fischer, Microfabrication of thermoelectric generators on flexible foil substrates as a power source for autonomous microsystems. J. Micromech. Microeng., 2001, 11, 146-152.

[18] I. Chowdhury, R. Prasher, K. Lofgreen, G. Chrysler, S. Narasimhan, R. Mahajan, D. Koester, R. Alley, R. Venkatasubramanian, "On-chip cooling by superlattice-based thin-film thermoelectrics". Nat. Nanotechnol., 2009, 4, 235-238.

[19] L.M. Goncalves, C. Couto, P. Alpuim, J.H. Correia. "Thermoelectric micro converters for cooling and energy-scavenging systems". J. Micromech. Microeng., 2008, 18, 064008 (5pp).

[20] J. Kurosaki, A. Yamamoto, S. Tanaka, J. Cannon, K. Miyazaki, H. Tsukamoto, "Fabrication and evaluation of a thermoelectric microdevice on a free-standing substrate". J. Electron. Mater., 2009, 38, 1326-1330.

[21] A. Boulouz, A. Giani, B. Sorli, L. Koutti, A. Massaq, F. Pascal-Delannoy. "Fabrication of Thermoelectric Sensor and Cooling Devices Based on Elaborated Bismuth-Telluride Alloy Thin Films". J. Mater. 2014, 2014, 30410 (8pp).

[22] G. Bulman, P. Barletta, J. Lewis, N. Baldasaro, M. Manno, A. Bar-Cohen, B. Yang. “Superlattice-based thin-film thermoelectric modules with high cooling fluxes”. Nat. Commun. 2016, 7, 10302.

[23] F. Yang, S. Zheng, H. Wang, W. Chu, Y. Dong. “A thin film thermoelectric device fabricated by a self-aligned shadow mask method”. J. Micromech. Microeng. 2017, 27, 055005.

[24] Böttner, H.; Nurnus, J.; Gavrikov, A.; Kuhner, G.; Jagle, M.; Kunzel, C.; Eberhard, D.; Plescher, G.; Schubert, A.; Schlereth, K. H. New thermoelectric components using microsystem technologies. J. Microelectromech. Syst. 2004, 13, 414.

[25] L.W. da Silva, M. Kaviany. “Fabrication and measured performance of a first-generation microthermoelectric cooler”. J. Memsci 2005, 14 (5), 1110.

[26] G.J. Snyder, J.R. Lim, C.-K. Huang, J.P. Fleurial. “Thermoelectric microdevice fabricated by a MEMS-like electrochemical process”. Nat. Mater. Lett. 2003, 2, 528-531.

[27] L.M. Goncalves, J.G. Rocha, C. Couto, P. Alpuim, J.H. Correia. “On-chip array of thermoelectric Peltier microcoolers”. Sensors and Actuators A 2008, 145-146, 75-80.

[28] T. Huesgen, P. Woias, N. Kockmann. “Design and fabrication of MEMS thermoelectric generators with high temperature efficiency”. Sensors and Actuators A 2008, 145-146, 423-429.

[29] L.M. Goncalves, “Materials, Preparation, and Characterization in Thermoelectrics”, Edited by D. M. Row, Chapter 19, 2012, Pages 1–19.

[30] C. Felser, A. Hirohata, *Heusler Alloys: Properties, Growth, Applications*. (Springer Series in Materials Science 2016, 222.

[31] M. Mikami, K. Kobayashi S.Tanaka. Power Generation Performance of Thermoelectric Module Consisting of Sb-Doped Heusler Fe_2VAl Sintered Alloy. Materials Transactions, 2011, 52, 8, pp. 1546-1548.

[32] M. Mikami, K. Kobayashi, T. Kawada, K. Kubo, N. Uchiyama. Development and Evaluation of High-Strength Fe_2VAl Thermoelectric Module. Japanese Journal of Applied Physics, 2008, 47, No. 3, pp. 1512–1516.

[33] H. Miyazaki, S. Tanaka, N. Ide, K. Soda, Y. Nishino, Thermoelectric properties of Heusler-type off-stoichiometric $Fe_2V_{1+x}Al_{1-x}$ alloys. Materials Research Express **1** (1), 015901 (2014)

[34] A. Diack-Rasselio, O. Rouleau, L. Coulomb, L. Georgeton, M. Beaudhuin, J.-C. Crivello, E. Alleno. Influence of Self-Substitution on the Thermoelectric Fe_2VAl Heusler Alloy. J. Alloys Compd., 2022, 920, No. 166037.

[35] F. Garmroudi, A. Riss, M. Parzer, N. Reumann, H. Müller, E. Bauer, S. Khmelevskyi, R. Podloucky, T. Mori, K. Tobita, Y. Katsura and K. Kimura, Boosting the thermoelectric performance of Fe_2VAl−type Heusler compounds by band engineering. Physical Review B 2021, **103** (8), 085202.

[36] E. Alleno, Review of the Thermoelectric Properties in Nanostructured Fe_2VAl. Metals, 2018, 8 (11), 864, pp1-7.

[37] D. Bourgault, H. Hajoum, S. Pairis, O. Leynaud, R. Haettel, J. F. Motte, O. Rouleau, E. Alleno. Improved Power Factor in Self-Substituted Fe_2VAl Thermoelectric Thin Films Prepared by Co-sputtering. ACS Appl. Energy. Mat., 2023, 6, 3, pp. 1526-1532.

[38] F. Garmroudi, M. Parzer, A. Riss, A. Ruban, S. Khmelevskyi, M. Reticcioli, M. Knopf, H. Michor, A. Pustogow, T. Mori, E. Bauer. Anderson Transition in Stoichiometric Fe_2VAl: High Thermoelectric Performance from Impurity Bands. Nat. Commun., 2022, 13, No. 3599.

[39] Y. Nishino, Y. Tamada. Doping Effects on Thermoelectric Properties of the Off-Stoichiometric Heusler Compounds $Fe_{2-x}V_{1+x}Al$. J. Appl. Phys., 2014, 115, No. 123707.

[40] D. Bourgault, C. Giroud-Garampon, N. Caillault, L. Carbone, J. A. Aymami. Thermoelectric Properties of n-Type $Bi_2Te_{2.7}Se_{0.3}$ and p-Type $Bi_{0.5}Sb_{1.5}Te_3$ Thin Films Deposited by Direct Current Magnetron Sputtering. Thin Solid Films, 2008, 516, 8579−8583.

[41] Cao, J.; Zheng, J.; Liu, H.; Tan, C.K.I.; Wang, X.; Wang, W.; Zhu, Q.; Li, Z.; Zhang, G.; Wu, J.; et al. Flexible Elemental Thermoelectrics with Ultra-High Power Density. Mater. Today Energy 2022, 25, 100964.

[42] Gao, W.; Liu, Z.; Baba, T.; Guo, Q.; Tang, D.; Kawamoto, N.; Bauer, E.; Tsujii, N.; Mori, T. Significant Off Stoichiometry Effect Leading to the N-Type Conduction and Ferromagnetic Properties in Titanium Doped Fe2VAl Thin Films. Acta Mater. 2020, 200, 848-856.

[43] N. Tsujii1, A. Nishide, J. Hayakawa, T. Mori. Observation of enhanced thermopower due to spin fluctuation in weak itinerant ferromagnet. Sci. Adv. 2019, 5, 5935.

[44] E. M. F. Vieira, A. L. Pires, J. P. B. Silva, V. H. Magalh~aes, J. Grilo et al. High-Performance μ-Thermoelectric Device Based on Bi_2Te_3/Sb_2Te_3 p−n Junctions. ACS Appl. Mater. Interfaces, 2019, 11 (42), 38946.

[45] S. J. Kim, J. H. We, B. J. Cho. A wearable thermoelectric generator fabricated on a glass fabric. Energy Environ. Sci., 2014, 7,1959.

[46] Madan, D.; Wang, Z.; Chen, A.; Juang, R.; Keist, J.; Wright, P. K.; Evans, J. W. Enhanced Performance of Dispenser Printed MA n-type Bi_2Te_3 Composite Thermoelectric Generators. ACS Appl. Mater. Interfaces 4 (2012) 6117−6124.

[47] Luo, J.; Cao, Z.; Yuan, M.; Chou, X. Preparation and testing of flexible thermoelectric power generator. Results Phys. 12 (2019) 1304− 1310.

[48] Yang, F.; Zheng, S.; Wang, H.; Chu, W.; Dong, Y. A thin film thermoelectric device fabricated by a self-aligned shadow mask method. J. Micromech. Microeng. 27 (2017) 055005.

[49] Francioso, L.; De Pascali, C.; Farella, I.; Martucci, C.; Creti, P.; Siciliano, P.; Perrone, A. In Flexible Thermoelectric Generator for Wearable Biometric Sensors, IEEE SENSORS 2010 Conference (2010) 747−750.

[50] Ao, D.W.; Liu,W.D.; Zheng, Z.H.; Shi, X.L.;Wei, M.; Zhong, Y.M.; Li, M.; Liang, G.X.; Fan, P.; Chen, Z.G. Assembly-Free Fabrication of High-Performance Flexible Inorganic Thin-

Film Thermoelectric Device Prepared by a Thermal Diffusion. Adv. Energy Mater. 12 (2022) 2202731 pp1-7.

[51] Rojas, J. P.; Conchouso, D.; Arevalo, A.; Singh, D.; Foulds, I. G.; Hussain, M. M. Paper-based origami flexible and foldable thermoelectric nanogenerator. Nano Energy 2017, 31, 296−301.

[52] H. Shang, C. Dun, Y. Deng, T. Li, Z, Gao, L. Xiao, H. Gu, D. J. Singh, Z. Ren, F. Ding. $Bi_{0.5}Sb_{1.5}Te_3$ -based films for flexible thermoelectric devices. J. Mater. Chem. A, 2020, 8, 4552-4561.

[53] M. Takashiri, T. Shirakawa, K. Miyazaki, H. Tsukamoto, Fabrication and characterization of bismuth–telluride-based alloy thin film thermoelectric generators by flash evaporation method, Sensors and Actuators A, 2007, 138, 329-334.

[54] H. Shang, Taiguang Li, D. Luo, Luo Yu, Q. Zou, Daxing Huang, Liye Xiao, H. Gu, Z. Ren, F. Ding. High-performance Ag-modified $Bi_{0.5}Sb_{1.5}Te_3$ films for the flexible thermoelectric generator. ACS Appl. Mater. Interfaces, 2020, 12, 7358-7365.

[55] Y. Li, J. Qiao, Y. Zhao, Q. Lan, P. Mao, J. Qiu, K. Tai, C. Liu, H. Cheng, A flexible thermoelectric device based on a Bi_2Te_3-carbon nanotube hybrid, J. Mater. Sci. Technol.2020, 58, 80.

[56] C. Li, F. Jiang, C. Liu, W. Wang, X. Li, T. Wang, J. Xu, A simple thermoelectric device based on inorganic/organic composite thin film for energy harvesting, Chem. Eng. J., 2017, 320, 201–210.

[57] J.H. We, S.J. Kim, B.J. Cho, Hybrid composite of screen-printed inorganic thermoelectric film and organic conducting polymer for flexible thermoelectric power generator, Energy, 2014, 73, 506–512.

[58] M. Kim, D. Park, J. Kim, Thermoelectric Generator Using Polyaniline-Coated Sb_2Se_3/Cu_2Se Flexible Thermoelectric Films. Polymers, 2021, 13, 1518 (pp1-11).

[59] Tian, R.; Wan, C.; Wang, Y.; Wei, Q.; Ishida, T.; Yamamoto, A.; Tsuruta, A.; Shin, W.; Li, S.; Koumoto, K. A Solution-Processed TiS2/Organic Hybrid Superlattice Film towards Flexible Thermoelectric Devices. J. Mater. Chem. A, 2017, 5, 564–570.

[60] L. Wang, Q. Yao, W. Shi, S. Qu, L. Chen, Engineering carrier scattering at the interfaces in polyaniline based nanocomposites for high thermoelectric performances. Mater. Chem. Front., 2017, 1, 741–748.

[61] Y. F. Ding, Y. Qiu, K. F. Cai, Q. Yao, S. Chen, L. D. Chen, J. Q. He. High performance n-type Ag_2Se film on nylon membrane for flexible thermoelectric power generator. Nat. Commun.,2019, 10, 841 pp1-7.

[62] Liang, J., Wang, T., Qiu, P., Yang, S., Ming, C., Chen, H., Song, Q., Zhao, K., Wei, T.-R., Ren, D. Flexible thermoelectrics: from silver chalcogenides to full-inorganic devices. Energy Environ. Sci., 2019, 12, 2983–2990.

[63] Gao Q, Wang W, Lu Y, Cai K, Li Y, Wang Z, Wu M., Huang C., He J. High power factor Ag/Ag_2Se composite films for flexible thermoelectric generators. ACS Appl Mater Interf 2021, 13(12), 14327–14333.

[64] S. Hou, Y. Liu, L. Yin, C. Chen, Z. Wu, J. Wang, Y. Luo, W. Xue, X. Liu, Q. Zhang, F. Cao. “High performance wearable thermoelectric generators using Ag_2Se films with large carrier mobility.” Nano Energy, 2021, 87, 106223 (pp1-8).

[65] S. Hou, Y. Liu, Y. Luo, X. Wang, L. Yin, X. Sun, Z. Wu, J. Wang, M. Li,Z. Chen, Y. Wang, J. Sui, J. Mao, X. Liu, Q. Zhang, F. Cao. “High-performance, thin-film thermoelectric generator with self-healing ability for body-heat harvesting.” Cell Rep. Phys. Sci.,2022, 3, 101146, pp1-13.

[66] Isotta, E.; Andrade, J.; Syafiq, U.; Jimenez, A.; Navarro, A.; Guc, M.; Saucedo Silva, Edgardo; Scardi, P. “Towards Low Cost and Sustainable Thin Film Thermoelectric Devices Based on Quaternary Chalcogenides.” Adv Funct Mat., 2022, 32, 2202157, pp1-12.